Advances in Aircraft and Spacecraft Science, *Vol. 7, No. 4 (2020) 371-385*
DOI: https://doi.org/10.12989/aas.2020.7.4.371

Drag reduction for payload fairing of satellite launch vehicle with aerospike in transonic and low supersonic speeds

R. C. Mehta*

Department of Aeronautical Engineering, Noorul Islam Centre for Higher Education, Kumaracoil 629180, India

(Received December 30, 2019, Revised May 24, 2020, Accepted June 6, 2020)

Abstract. A forward-facing aerospike attached to a payload fairing of a satellite launch vehicle significantly alters its flowfield and decreases the aerodynamic drag in transonic and low supersonic speeds. The present payload fairing is an axisymmetric configuration and consists of a blunt-nosed body along with a conical section, payload shroud, boat tail and followed by a booster. The main purpose of the present numerical simulations is to evaluate flowfield and assess the performance of aerodynamic drag coefficient with and without aerospike attached to a payload fairing of a typical satellite launch vehicle in freestream Mach number range $0.8 \leq M_\infty \leq 3.0$ and freestream Reynolds number range $33.35 \times 10^6/\text{m} \leq Re_\infty \leq 46.75 \times 10^6/\text{m}$ which includes the maximum aerodynamic drag and maximum dynamic conditions during ascent flight trajectory of the satellite launch vehicle. A numerical simulation has been carried out to solve time-dependent compressible turbulent axisymmetric Reynolds-averaged Navier-Stokes equations. The closure of the system of equations is achieved using the Baldwin-Lomax turbulence model. The aerodynamic drag reduction mechanism is analysed employing numerical results such as velocity vector plots, density and Mach contours in conjunction with the experimental flow visualization pictures. The variations of wall pressure coefficient over the payload fairing with and without aerospike are exhibiting different kind of flowfield characteristics in the transonic and low supersonic speeds. The numerically computed results are compared with schlieren pictures, oil flow patterns and measured wall pressure distributions and exhibit good agreement between them.

Keywords: aerodynamics drag coefficient; aerospike; blunt-nose body; payload fairing; CFD simulation; fluid dynamics; transonic flow; supersonic flow; shock wave; satellite launch vehicle

1. Introduction

The main aerodynamic purpose of a payload fairing in any satellite launch vehicle is to protect payload from the internal and external environments such as aerodynamic forces and heating, acoustics, vibration, contaminations etc. The payload fairing is jettisoned once the vehicle reaches out of the atmosphere. A compressible boundary layer is developed along a payload fairing in the absence of a forward facing aerospike. The forebody region of the payload fairing is characterized by formation of a bow shock wave for Mach number greater than one that decelerates the supersonic flow and causes high values of pressure, density and temperature behind the bow shock wave. Thus, the aerodynamic drag increases due to the wave drag. Propulsive power requirement

*Corresponding author, Professor, E-mail: drrakhab.mehta@gmail.com

http://www.techno-press.org/?journal=aas&subpage=7 ISSN: 2287-528X (Print), 2287-5271 (Online)

of a satellite launch vehicle depends on the aerodynamic drag experienced by the payload fairing. An aerospike attached to a payload fairing creates a recirculation region of separated flow (Daniels *et al.* 1954) over the forward region of the payload fairing that reduces the aerodynamic drag due to the reduced dynamic pressure in transonic and low supersonic Mach number range. The M-3S-II rockets and the Trident I and II missiles have a fixed aerospike to reduce aerodynamic drag during its ascent trajectory. An Aerospike is also employed in the orbiter of space shuttle to measure angle of incidence during the ascent phase of the flight (Hillje and Nelson 1993).

The experimental investigations have been reported by Chang (1970) for axially symmetric models with nose shapes of hemispheres, flat surfaces, hemispherical flats, ogives and tapered configurations, and cylindrical after bodies in the freestream Mach number range $1.75 \leq M_\infty \leq 14.0$ and Reynolds number $0.86 \times 10^6 \leq Re_D \leq 1.5 \times 10^6$ based upon the blunt after body diameter. Chung *et al.* (2014) investigated influence of flow expansion and compression in the transonic regime. An experimental study on bodies of revolution with flat and hemispherical nose shapes and with and without thin protruded probes of different length was carried out Mair (1952) for Mach 1.96. Spiked axisymmetric forebodies of specific forebody were experimentally found in free flight at Mach number range 0.7 to 1.3**,** to be aerodynamically beneficial and practical (Piland and Putland 1954). Haupt and Koenig (1987) have conducted an experimental study on spike-induced flow separation at transonic Mach numbers on blunt body. Mehta *et al.* (1997) presented numerical analysis of separated flow over a aerospike attached to payload fairing in the range of M_∞ of $1.5 \leq M_\infty \leq 3.0$.

Menezes *et al.* (2009) have carried out experiment in a shock-tunnel on large blunt-nosed cone with spike attachments flying at hypersonic speed. Ahmed and Qin (2010a) have analyzed drag reduction using aerodiscs for hypersonic hemispherical body vehicle. In a review article published by Ahmed and Qin (2011b) provides advances in the aerothermodynamics of spiked bodies at high speeds and pointed out some areas for further investigation. Yadav *et al.* (2013) have developed the concept of double-disk aerospikes, which favourably reduced reattachment aerodynamic drag and heat flux on the blunt body. The flowfields over a blunt cone with and without aerodisk at hypersonic speeds are investigated by Huang *et al.* (2017a). Gerdroodbary *et al.* (2010) have investigated effectiveness of aerodisk/aerospike assemblies as retractable drag reduction devices for large angle blunt cones operated at Mach 5.75. Deng *et al.* (2017) have investigated the pressure distribution and aerodynamic drag characteristics by simulating and comparing the lifting body with or without the aerospike at Mach 8. Sebastian *et al.* (2016) have numerically analyzed performance at Mach 6 and different length-to-diameter ratio at different angle**s** of attack. Flow over blunt body with spike at hypersonic speeds have been extensively studied in last few decades and reviewed by Huang *et al.* (2019b).

Experimental and numerical studies have been made by Venkateshan *et al.* (2011) using spikes of different shapes mounted on a hemispherical blunt body at $M_\infty = 2.0$. Flow visualization employing differential interferometry and pressure measurements on spike-tipped bodies at $M_\infty = 3.5$ is analyzed by Srulijes *et al.* (2000). Milicov and Parlevic (2002) experimentally measured aerodynamic coefficients of spike attached to blunt-nosed bodies at $M_\infty = 1.89$. Studies reported by White (1993) gives the details of the flowfield on blunt bodies of different shapes at supersonic speed in the presence of various types of spikes. Yamauchi *et al.* (1995) numerically investigated the flowfield around a spiked blunt body at $M_\infty = 2.1$, 4.15 and 6.80. Shoemaker (1990) computed flowfield over family of spikes with bi-conic nose-tip with hemispherical nose at $M_\infty = 2.5$ with experimental validation. Mikhail (1991) numerically simulated flowfield over spike-nosed projectile at $M_\infty = 1.72$ at zero angle of attack. Jones (1952) measured drag with a balance for

different bluntness ratio bodies at $M_\infty = 2.72$ and Reynolds number 1.83 x 10^6 at zero-degree angle of incidence. They found that the drag is increasing with the bluntness of the body and it is a minimum value if the nose radius is more than 0.25 of radius of blunt body. Drag reduction of a hemispherical body adopting spike at supersonic speed has been studied by Das *et al.* (2013). A review paper presented by Wang *et al.* (2016) have reviewed various types including aerospike attached to the blunt body to reduce aerodynamic drag at high speeds. Most of the experimental investigations have attempted to determine the critical length of the spike at supersonic speeds in order to reduce the wave drag.

It appears that transonic flow past probes is a subject of only a limited number of experimental and numerical studies in the open literature. Therefore a definite conclusion regarding the flow aspects of an aerospike attached to a payload fairing cannot be reached easily at transonic and supersonic Mach numbers.

A schematic sketch for the flowfield is shown in Fig. 1 which is based on the observation of velocity vector and density contour plots in the vicinity of an aerospike attached to a blunt-nose body at transonic and supersonic speeds (Mehta 2010a). Flowfield over without and with an aerospike attached to a payload fairing of a typical satellite launch vehicle is delineated in Fig. 1(a) and (b) respectively for transonic speed. Fig. 1(a) shows the growth of compressible boundary layer on the payload fairing starting from the stagnation point. A recirculation flow region over the aerospike appears as depicted in Fig. 1(b) and flow becomes complex as compared to the without aerospike as shown in Fig. 1(a). The flow separation and recirculation region on the aerospike contributes to the reduction in wall pressure which is a function of freestream Mach numbers. The boundary layer is distinctly different without and with an aerospike mounted on the payload fairing as seen in Fig. 1(a) and (b) for $M_\infty < 1$.

Fig. 1(c) and 1(d) depicts the flowfield over without and with an aerospike attached to payload fairing, respectively, for $M_\infty > 1$. The location of the stagnation point is also marked in Fig. 1. The flowfield is characterized by a formation of the bow shock wave in front of the spike, a separated flow region and interaction between the bow shock wave and the reattachment shock wave. The features of the high-speed flowfield are based on experimental (Kalimuthu *et al.* 2019) and numerical (Mehta 2010a) and (Yamauchi *et al.* 1995) studies. For the $M_\infty < 1$ case, a shear layer is formed, and it contains a recirculation region. Fig. 1(c) and (d) shows flowfield characteristics for the supersonic case such as formation of bow shock wave on the blunt nose of the payload fairing. The bow shock wave is enclosed by a subsonic-supersonic region between them. A well-known remedy for reducing the effect of the bow shock wave on a blunt body, while keeping a blunt nose, is mounting the aerospike on the blunt-nose payload fairing. The simplest aerospike design is a conical aerospike mounted on the tip of a blunt body as depicted in Fig. 1(d). The ideal case would be that the boundary layer separates along the whole aerospike surface due to the pressure rise over the bow shock wave. The separated boundary layer forms a shear layer that reattaches on the blunt nose. Due to the shear layer, the outer supersonic bow is detected and a weaker conical shock is formed instead of the initial bow shock. The conical shock wave unites with the reattachment shock wave further downstream. A recirculation zone forms inside the shear surface and shows significantly lower pressure levels compared with the blunt body without the aerospike. The flow separation zone is noticed around the root of the spike up to the reattachment point of the flow at the corner of the blunt body. Due to the recirculating region, the pressure at the stagnation region of the blunt body will reduce. However, because of the reattachment of the shear layer on the corner of the blunt-body, the pressure near the reattachment point becomes large. The spike is characterized by a free shear layer, which is formed as a result of the flow separating from the

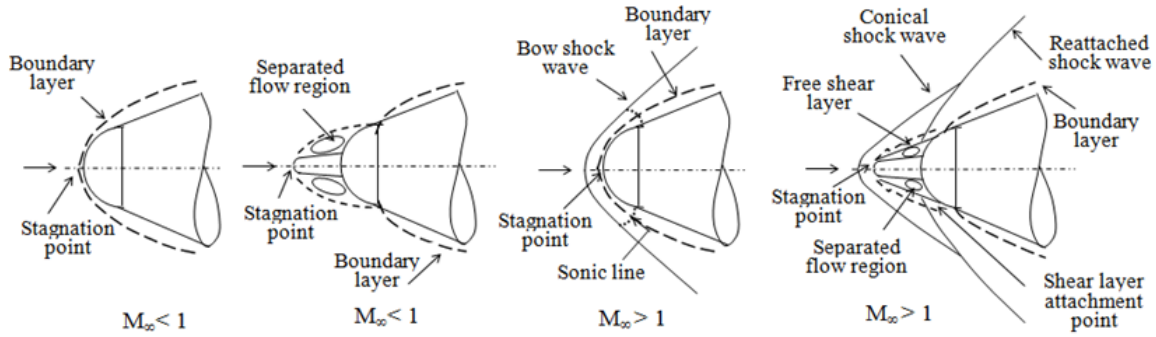

Fig. 1 Schematic sketches of flowfield over payload fairing (a) without aerospike $M_\infty < 1$, (b) with aerospike $M_\infty < 1$, (c) without aerospike $M_\infty > 1$ and (d) with aerospike $M_\infty > 1$

spike's leading edge and reattaching to the blunt body. The separated boundary layer forms a shear layer that reattaches on the blunt nose body.

In the present work, numerical analysis in conjunction with experimental data has been used to analyze the complex fluid mechanism of payload fairing without and with aerospike of a typical satellite launch vehicle. Experimental data is available in the form of schlieren pictures, oil flow patterns and measurement of surface pressure distribution. A computational fluid dynamics approach is considered here to investigate drag reducing mechanism in the presence of an aerospike on a typical payload fairing of satellite launch vehicle. The time-dependent compressible turbulent Reynolds-averaged Navier-Stokes equations are solved using a finite volume spatial discretization in conjunction with temporal integration employing three-stage Runge-Kutta time-stepping scheme. The flow characteristics are investigated in the Mach number range $0.8 < M_\infty < 3.0$ and freestream Reynolds number range $33.35 \times 10^6/\text{m} \leq Re \leq 46.75 \times 10^6/\text{m}$. The numerical results are analysed in the subsequent sections in order to investigate the drag reduction mechanism due to the aerospike attached to the payload fairing.

2. Numerical analysis

2.1 Governing equations

The high-speed flow over the aerospike attached to the payload fairing is considered as axisymmetric at zero angle of incidence. Hence, axisymmetric compressible turbulent Reynolds-averaged Navier-Stokes equations (RANS) in the conservation form of mass, momentum and energy equations are expressed by

$$\frac{\partial \boldsymbol{U}}{\partial t} + \frac{\partial \boldsymbol{F}}{\partial x} + \frac{1}{r}\frac{\partial (r\boldsymbol{G})}{\partial r} = \frac{H}{r} \tag{1}$$

where the vector of conservative variables $\boldsymbol{U}$, the convective vector fluxes $\boldsymbol{F}$ and $\boldsymbol{G}$, and the source term $\boldsymbol{H}$ are defined as

$$\boldsymbol{U}=\begin{bmatrix}\rho\\ \rho u\\ \rho v\\ \rho e\end{bmatrix},\quad \boldsymbol{F}=\begin{bmatrix}\rho u\\ \rho u^2-\sigma_{xx}\\ \rho uv-\sigma_{xr}\\ (\rho e-\sigma_{xx})u-\sigma_{xr}+q_x\end{bmatrix},\quad \boldsymbol{G}=\begin{bmatrix}\rho v\\ \rho uv-\sigma_{xr}\\ \rho v^2-\sigma_{rr}\\ (\rho e-\sigma_{rr})v-\sigma_{rx}+q_r\end{bmatrix},\quad \boldsymbol{H}=\begin{bmatrix}0\\ 0\\ -\sigma_+\\ 0\end{bmatrix} \tag{2}$$

where σ_{xx}, σ_{rx}, σ_{xr}, σ_{rr} are components of the stress vectors, q_x and q_r are components of the heat flux vectors. Reynolds stresses and turbulent heat fluxes in the mean flow equations are modeled by introducing an isotropic eddy viscosity μ_t and a turbulent Prandtl number Pr_t and are assumed to take a constant value of 0.72 and 0.90, respectively. Thus, the viscous terms in Eq. (2) become

$$\sigma_{xx}=-\frac{2}{3}(\mu+\mu_t)\nabla\cdot\phi+2(\mu+\mu_t)\frac{\partial u}{\partial x},\qquad \sigma_{rr}=-\frac{2}{3}(\mu+\mu_t)\nabla\cdot\phi+2(\mu+\mu_t)\frac{\partial v}{\partial r}$$

$$\sigma_{xr}=(\mu+\mu_t)\left(\frac{\partial u}{\partial r}+\frac{\partial v}{\partial x}\right),\quad \sigma_+=-p-\frac{2}{3}(\mu+\mu_t)\nabla\cdot\phi+2(\mu+\mu_t)\frac{v}{r} \tag{3}$$

$$\nabla\cdot\phi=\frac{\partial u}{\partial x}+\frac{\partial v}{\partial r}+\frac{v}{r},\quad q_x=-Cp\left(\frac{\mu}{Pr}+\frac{\mu_t}{Pr_t}\right)\frac{\partial T}{\partial x},\qquad q_r=-Cp\left(\frac{\mu}{Pr}+\frac{\mu_t}{Pr_t}\right)\frac{\partial T}{\partial r}$$

The coefficient of molecular viscosity is evaluated employing Sutherland's formula; T is related to p and ρ by perfect gas equation of state as

$$p=\rho(\gamma-1)\left[e-0.5\left(u^2+v^2\right)\right] \tag{4}$$

The ratio of the specific heats γ was assumed constant value and $\gamma = 1.4$. For the turbulent flow situations, the closure of the system of equations is achieved by introducing the Baldwin-Lomax (1978) turbulence model. The algebraic model utilizes the vorticity distribution to determine the scale length, has been extensively used in conjunction with the RANS equations (Mehta 1997) and is reputed to yield acceptable engineering solution (Purohit 1986).

To simplify the spatial discretization in numerical technique, Eq. (1) can be written in the integral form over a finite computational domain Ω with the boundary of the domain Γ as

$$\frac{d}{dt}\int_\Omega \boldsymbol{U}d\Omega+\int_\Gamma(\boldsymbol{F}dr-\boldsymbol{G}dx)-\int_\Omega \boldsymbol{H}d\Omega=0 \tag{5}$$

The contour integration around the boundary of the cell is performed in anticlockwise sense in order to keep flux vectors normal to boundary of the cell. The computational domain Ω has a finite number of non-overlapping quadrilateral cells. The conservation variables within the computational cell are represented by their average values at the cell centre.

The inviscid fluxes are computed at the cell-centre resulting in flux balance. The summation is carried out over the four edges of the cell. The derivatives of primitive variables in the viscous flux are evaluated by using the method of lines. In the cell-centred spatial discretization scheme is non-dissipative, therefore, artificial dissipation terms (Jameson *et al.* 1981) are added by blending of second and fourth differences of the vector conserved variables. The blend of second and fourth

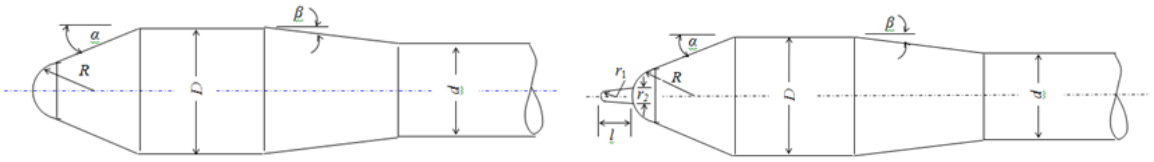

(a) (b)

Fig. 2 (a) geometrical detail of the payload fairing without aerospike and (b) with the forward-facing aerospike

Table 1 Freestream conditions

M_∞	$p_\infty \times 10^5$ Pa	T_∞ K
0.80	0.83	265
0.90	0.787	258
0.95	0.766	254
1.00	0.73	250
1.20	0.64	232
1.50	0.45	207
1.70	0.36	186
2.00	0.285	166
3.00	0.122	107

differences provides third order background dissipation in smooth region of the flow and first-order dissipation in shock waves.

The spatial discretization described above reduces the integral equation to semi-discrete ordinary differential equations. Eq. (5) is numerically integrated using multi-stage Runge-Kutta time stepping scheme of Jameson *et al.* (1981). The numerical algorithm is second-order accurate in space discretization and time integration. The scheme is stable for a Courant number ≤ 2. Local time steps are used to accelerate to a steady-state solution by setting the time step at each point to the maximum value allowed by the local Courant-Friedrichs-Lewy condition.

2.2 Initial and boundary conditions

At transonic freestream Mach number, the computational domain of dependence is unbounded, and the implementation of boundary and initial condition become critical, the known physically acceptance of far-field boundary conditions usually limit the flow variables to asymptotic values at large distance from the payload fairing. On the other hand, adjustment of the grid points spacing to the body demands fine dimensions to yield reasonable resolution of the boundary layer. Therefore, suitable coordinate stretching and placement of the far-field boundary condition must be performed in numerical simulations. The freestream conditions are prescribed on the outer boundary. On the payload fairing wall, no-slip and adiabatic conditions are imposed. At the line of symmetry ahead of the payload fairing an image cell is imposed on the solved variables. At the inflow, all the flow variables are taken at the freestream values as tabulated in Table 1.

For the transonic flow, non-reflecting far-field boundary conditions are applied at the outer boundary of the computational domain. For supersonic flow, all of the flow variables are

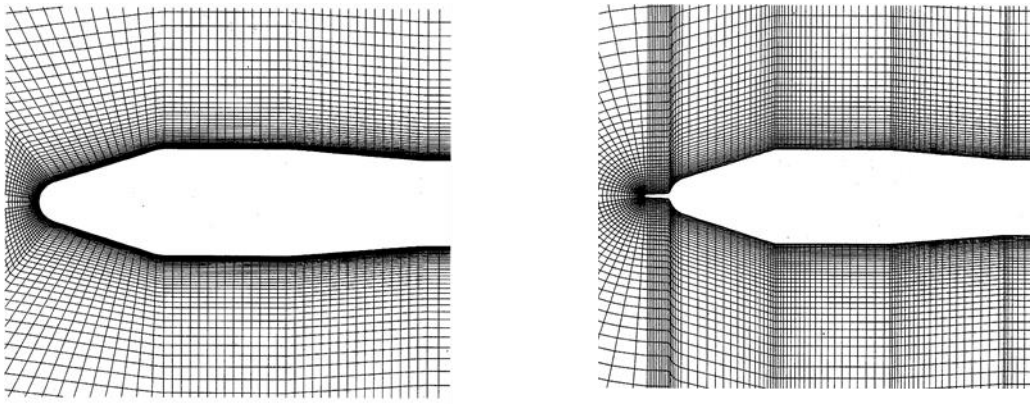

(a) (b)

Fig. 3 Geometrical detail of the payload fairing (a) without aerospike and (b) with forward-facing aerospike

extrapolated from the vector of conserved variables $\boldsymbol{U}$. At the line of symmetry ahead of the, an image cell is imposed to the solved variables.

2.3 Payload fairing geometry and computational grid

Fig. 2(a) and 2(b) depicts the nomenclature of geometrical parameters of payload fairing without and with aerospike, respectively. The maximum diameter of the payload shroud is D and the booster diameter is d as shown in Fig. 2. The spherical cap of the payload fairing is R. The fore body maximum diameter of the model is 43.26 mm, whereas the booster diameter is 35 mm. The spherical cap radius is 8.75 mm. For the blunt-nosed cone, the inclination at the fore body is α in degree and its value is 20^{o}. The boat tail angle is β in degree measured clockwise from the axis with reference of the oncoming flow direction and is 5.5^{o}.

The hemispherical nose of forward-facing aerospike has a radius r_2 = 0.55 mm and length l = 10 mm. The other end of the spike has r_1 = 49 mm and is attached to the forward facing blunt spherical cap of the payload fairing. These subscale dimensions are chosen after considering the blockage and compatibility condition with the model system support of wind tunnel.

The body-oriented grids are generated using a homotopy scheme in conjunction with finite element method (Mehta 2017). The stretched grids are generated in an orderly manner. A non-uniform and non-overlapping structured grid is generated for numerical simulations. The grid-stretching factor is selected as 5, and the outer boundary of the computational domain is maintained as 3.5-4.5 times maximum diameter D of the payload fairing. In the downstream direction, the computational boundary is about 6-9 times the diameter of the module; D. Fig. 3(a) and 3(b) show axisymmetric view of grid over the payload fairing without and with aerospike, respectively. The grid arrangement is found to yield a relative difference of about ± 3% in the pressure peak, which is in the same range as the pressure measurement error in the wind tunnel with a blockage ratio of about 0.3%. The convergence criterion is based on the difference in density values at any of the grid points, between two successive iterations $\left|\rho^{n+1}-\rho^{n}\right| \leq 10^{-5}$ where n is time-step counter. The numerical computations were carried out with different grid arrangements in order to get a grid independency check (Mehta 2010b). The computation is performed using 132 × 62 and 152 × 62 grid points without and with aerospike payload fairing.

The finer grid near the wall helps to resolve the boundary layer. The coarse grid economizes the computer time. The minimum grid size in the normal direction of the payload fairing is about 1.70×10^{-4} m.

3. Results and discussion

The above numerical algorithm is used to obtain the flowfield over the aerospike attached to the payload fairing of satellite launch vehicle. The current experimental data consists of schlieren pictures, oil flow patterns and surface pressure distributions. An initial comparison with available experimental data is made for the case without forward facing aerospike. This procedure will establish the overall credibility of the numerical solver as well as guidelines for subsequent study.

3.1 Flowfield visualization and characteristics

Fig. 4 depicts the velocity vector plots over the payload fairing at freestream Mach number 1.0 and 1.5. Fig. 4(a) shows formation of recirculation region, shear layer and boundary layer at M_∞ = 1.0. Fig. 4(b) and 4(c) exhibits close-up view of the velocity vector plots without and with aerospike attached to payload fairing, respectively, at M_∞ = 1.5. It is important to mention here that the flowfield is significantly altered over the payload fairing in presence of the aerospike. The fore-body is having subsonic flow enclosed with a sonic line as seen in Fig. 4(b). Fig. 4(b) and 4(c) shows effect of the without and with aerospike for M_∞ = 1.5, respectively, over the payload fairing. For $M_\infty > 1.0$, a bow shock is formed which causes high surface pressure on the blunt-nose payload fairing. A detached bow shock wave is formed in front of the payload fairing which is also having practically normal shock to the payload fairing axis. The flow behind the shock wave is subsonic; the shock wave is no longer independent of the far-downstream conditions. The effect of freestream Mach number over the separation in the aerospike region can easily be noticed in the velocity vector plots. A large separated flow region is occurred in front of the payload fairing and the shear layer, and the boundary of the separated region is clearly observed in Fig. 4(c). A zoomed view of the velocity vector plots is depicted in Fig. 4(c) shows all the essential flow features for M_∞ = 1.5. The reflected reattachment wave and the shear layer interacting are seen behind the reattachment shock wave. A strong recirculation flow can be seen distinctly over the aerospike. A close-up view of the velocity vector plots demonstrated that the drag reduction is attributed to the formation of a strong recirculation region of low velocity. We marked all the essential key flowfield features in Fig. 4(c) such as compression wave, recirculation region and shear layer in the vector plots. The fore-body of the aerospike is completely enveloped within the recirculation region. As the Mach number increases the dominance of the aerospike-induced separation grows for $M_\infty < 1$. Reattachment moves aft on the payload fairing and the separation angle becomes steeper for $M_\infty > 1$.

The separated shear layer and the recompression shock wave from the reattachment point on the shoulder of the hemispherical cap are visible. The fore-body of the aerospike is completely enveloped within the recirculation region. For $M_\infty > 1.0$, a bow shock wave is formed which causes high surface pressure on the blunt-nose payload fairing. The effect of freestream Mach number over the separation in the aerospike region can easily be noticed in the velocity vector plots. As the Mach number increases the dominance of the aerospike-induced separation grows for $M_\infty < 1$. Reattachment moves aft on the payload fairing and the separation angle becomes steeper

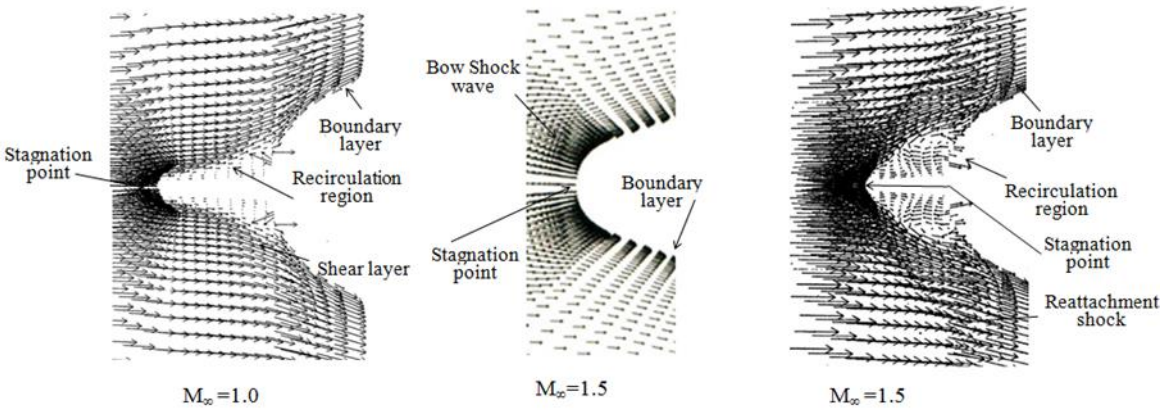

(a) (b) (c)

Fig. 4 (a) Enlarged view of vector plots at M_∞ = 1.0, (b) flowfield over the payload fairing without arerospike M_∞ = 1.5 and (c) with aerospike at M_∞ = 1.5

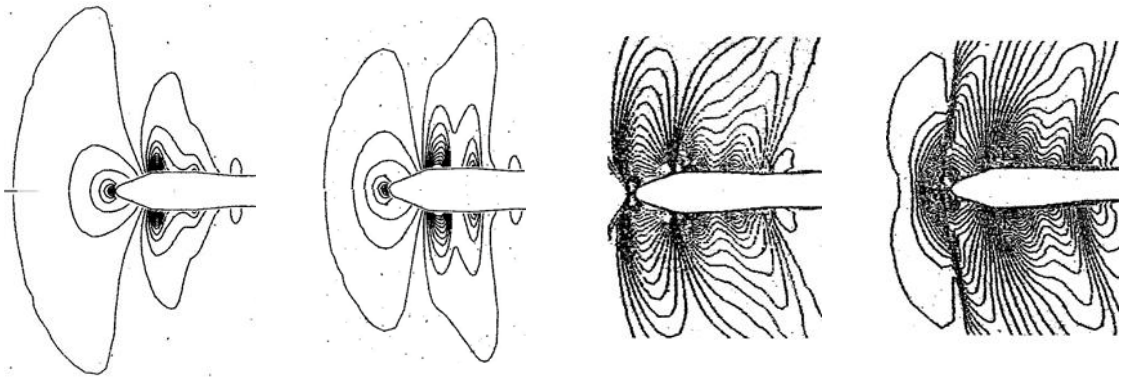

(a) (b) (c) (d)

Fig. 5 Density contour without aerospike at (a) M_∞ = 0.8, (b) M_∞ = 0.9, (c) M_∞ = 1.0 and (d) with aerospike at M_∞ = 1.0

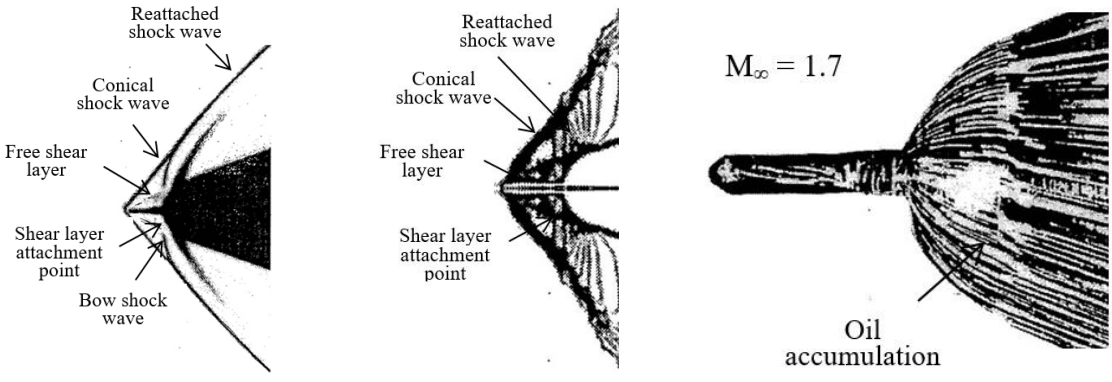

(a) (b) (c)

Fig. 6 Close-up view of (a) schlieren picture over payload fairing with aerospike M_∞ = 1.5, (b) density contour plots M_∞ = 1.5 and (c) oil flow over aerospike M_∞ = 1.7

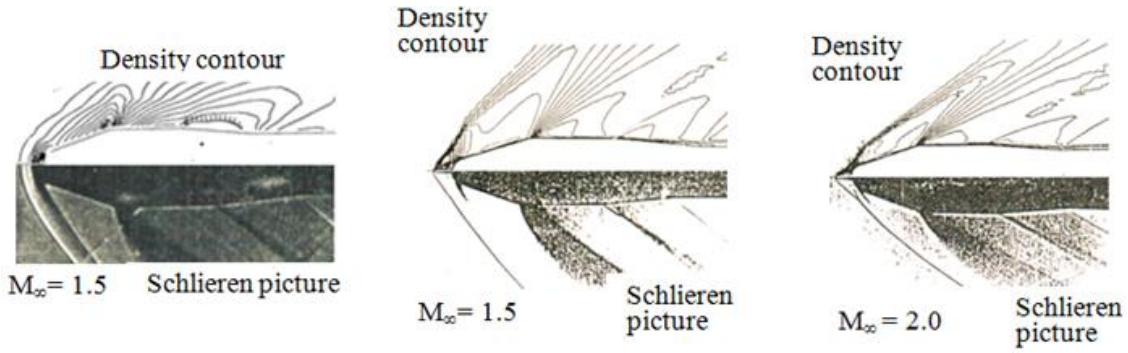

(a) (b) (c)

Fig. 7 Density contours and schlieren picture over payload fairing (a) without aerospike M_∞ = 1.5, (b) with aerospike M_∞ = 1.5 and (c) with aerospike M_∞ = 2.0

for $M_\infty > 1$. Unsteady flow is observed ahead of a variety of axisymmetric forebodies attached with spiked/aerodisk flying especially at supersonic and hypersonic speeds (Panaras and Drikakis 2009). The residual error norms were found oscillating at some time level of iteration on the aerospike case as compared to the without aerospike case (Mehta 2002). The main focus of the present analysis is to investigate the drag reduction mechanism and its benefit on the aerodynamic drag in Mach number range of $0.8 \leq M_\infty \leq 3.0$. This is attributed to the flow in the vicinity of the spike containing vorticity of the separated region (Saho *et al.* 2016) and needs global time-stepping in the numerical simulation.

Fig. 5(a)-5(c) shows density contour plots over the payload fairing without aerospike for M_∞ = 0.8, 0.9 and 1.0, respectively. The density contours capture all the essential flowfield features of transonic speeds. Fig. 5(d) displays the density contours over the payload fairing with the aerospike at M_∞ = 1.0. It is interesting to note from Fig. 5(c) and (d) that the flowfield entirely altered due to the aerospike ahead of the payload fairing at M_∞ = 1.0.

The enlarged view of the schlieren picture and density contour plots are shown in Fig. 6(a) and (*b*) for M_∞ = 1.5. The schlieren pictures reveal the flowfield behaviour over the aerospike and also the drag reduction mechanism due to the interaction of the shock waves which are a function of freestream Mach number. The numerical simulations captured all the essential flow features and compared well with the schlieren picture. A mixture of titanium dioxide, oleic acid, and high-vacuum oil in suitable proportions was sprayed on the model before a run. The streamline patterns obtained were photographed just after run. The model was painted black to obtain good contrast. Fig. 6(c) shows the oil flow pattern for the aerospike at zero angle of attack. It is seen from the figure that at zero angle of attack, the positive pressure zone is symmetric around the axis. The oil flow picture at M_∞ = 1.7 also shows accumulation of oil which has a predicted confirms result from our numerical analysis.

The density contour plots of the flowfield around the payload fairing without and with aerospike attached to the satellite launch vehicle are shown in Fig. 7. We compared them against corresponding schlieren photographs. Formation of the bow shock wave can be observed in the case of payload fairing without aerospike in Fig. 7(a). The computed flowfields show good agreement with the schlieren photographs. The above flowfield characteristics reveals that the flowfield features altered as the freestream Mach number change from transonic to low supersonic speeds.

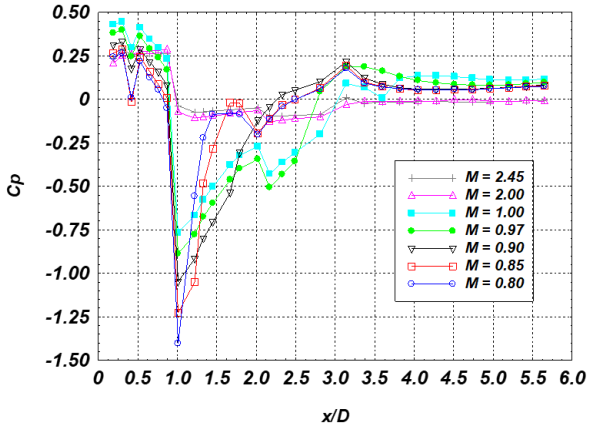

Fig. 8 Variation of surface pressure coefficients along the payload fairing without forward-facing aerospike

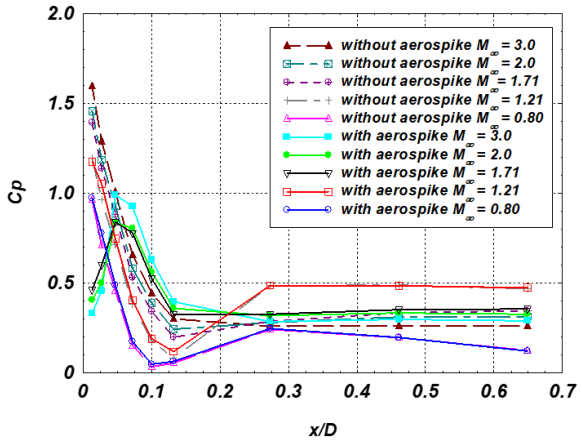

Fig. 9 Variation of wall pressure coefficients on the spherical cap of payload fairing with and without aerospike

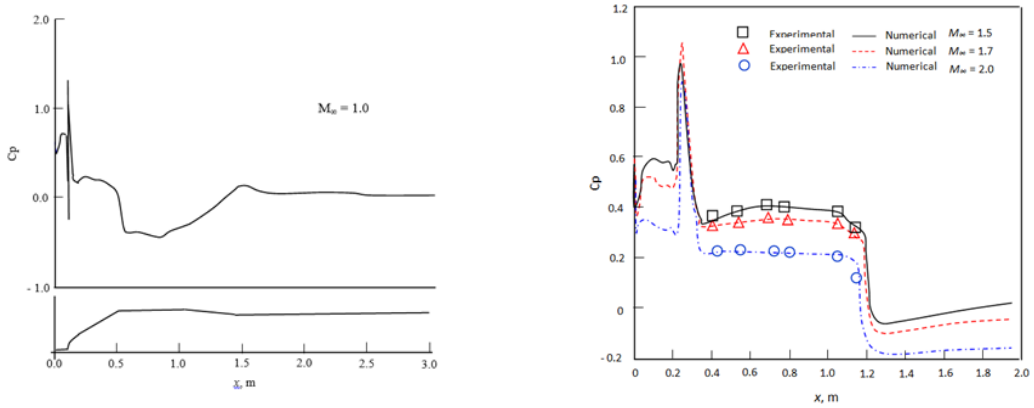

(a) (b)

Fig. 10 (a) Variation of computed (a) computed pressure coefficients along the payload fairing with the forward-facing aerospike for M_∞ = 1.0 and (b) for M_∞ = 1.5, 1.7 and 2.0

3.2 Surface pressure over payload fairing

The pressure coefficient $Cp = [(p_s - p_\infty)/q_\infty]$ variations along the payload fairing (x/D) without aerospike for Mach number range $0.8 < M_\infty < 3.0$ are shown in Fig. 8. Where p_s is the wall pressure, p_∞ is freestream pressure and q_∞ is freestream dynamic pressure. The pressure profile displays the transonic flow behaviour. The Cp variation changes in the supersonic speeds due to formation of bow shock waves, expansion and compression on the shoulder points of the payload shroud. Numerical result is found in good agreement with experimental data (Mehta 1997).

The computed and measured pressure coefficients without and with the aerospike on the blunt-nose body of payload fairing of a typical satellite launch vehicle is shown in Fig. 9. The wall pressure measurement ports are shown as marked in Fig. 9. Pressure measurement model has a provision to attach the aerospike at the hemispherical-conical body of the payload fairing. There are five pressure ports on the blunt-nose portion of the payload fairing to measure the surface pressure with and without aerospike. These pressure measurements reveal the effect of the attached aerospike on the payload fairing and influence of freestream Mach number. The error of all pressure transducer is within the ± 0.51% of maximum value of pressure range. In general, good agreement is obtained between the present computations and the available experiment data. The pressure over the payload fairing is significantly altered when an aerospike is attached to the payload fairing. To quantify the pressure field over the payload fairing with and without aerospike, the pressure distribution over the blunt nose was measured at zero angle of attack and compared with the numerical results for different freestream Mach number in Fig. 9. It is important to note that for $M_\infty < 1$ that the reduction of surface pressure is not minor. A significant drop of surface pressure is found for $M_\infty > 1$ which is coincidence as discussed in the above velocity vector plots Fig. 6 in the presence of the aerospike at $M_\infty = 1.5$. The aerospike causes the pressure levels over the payload fairing cap decrease with increase freestream Mach number.

Fig. 10 (a) depicts numerically computed variation of pressure coefficient along the payload fairing with forward-facing aerospike at $M_\infty = 1.0$. In the figure, the axial distance x is measured from the stagnation point of the payload fairing, and $x = 0$ is defined as the stagnation point. The reattachment shock wave on the payload fairing causes a spike in the wall pressure coefficient. It is interesting to note that there is no pressure jump in the case of without forwarding-facing aerospike attached to the payload fairing as shown in Fig. 8. This is attributed to reattach shock wave impinging on the payload fairing. The characteristics of the flowfield at $M_\infty = 1.0$ is as observed in Figs. 4(a) and 5(d). Fig. 10(b) shows the variation of pressure coefficient along the payload fairing with forward-facing aerospike for $M_\infty = 1.5$, 1.7 and 2.0. It can be observed from the figure that the pressure coefficient Cp decreases progressively as the M_∞ increases. The experimental data of pressure coefficient are compared with numerical results. It is important to mention here that scale of Cp with aerospike is changed as seen without aerospike in Fig. 8. The reattachment shock wave on the payload fairing gives corresponding spike in the pressure coefficient. The agreement with the experimental results is good.

3.3 Aerodynamic drag

The drag reduction capabilities of the aerospike on a payload fairing of typical satellite launch vehicle are of interest in the present numerical analysis. Aerodynamic drag coefficients for configuration with and without aerospike are computed from the above-mentioned numerical method. The drag coefficients without aerospike $C_{D,ws}$ and with aerospike $C_{D,s}$ are presented in

Table 2 Aerodynamic drag coefficient without and with aerospike

M_∞	C_D		$\{(C_{D,ws} - C_{D,s})/ C_{D,ws}\}\%$
	$C_{D,ws}$	$C_{D,s}$	
0.80	0.116	0.095	18.10
0.85	0.180	0.146	18.89
0.90	0.235	0.190	19.15
0.95	0.295	0.235	20.33
1.00	0.344	0.269	21.80
1.20	0.510	0.375	22.54
1.50	0.495	0.325	24.24
1.70	0.462	0.325	29.65
2.00	0.351	0.223	36.47

Table 2. It can be seen from the table that the percentage reduction in aerodynamic drag occurs at $M_\infty = 1.2$. The reduction when $M_\infty < 1$ is different with respect to $M_\infty > 1$. Thus, the trend in the reduction of C_D coincides with the above numerically simulated flowfield behaviour. The aero-spiked payload fairing drag coefficient is less than the corresponding without aero-spiked drag coefficient at any Mach number. The key reason of the drag reduction is the pressure distribution on the payload fairing, especially near the nose of the blunt body of payload fairing. The pressure in the vicinity of the blunt-nose body is low because of the flow separation existing under all freestream Mach numbers as exhibited in the velocity vector and density contour plots.

4. Conclusions

A computational fluid dynamics simulation over a payload fairing of satellite launch vehicle with and without aerospike is carried out by solving time-dependent compressible turbulent axisymmetric Navier-Stokes equations. The closure of the system of equations is achieved using an algebraic turbulence model. The numerical simulation is performed on a single-block structured computational domain. The flowfields over the aerospike depend on freestream Mach number. Effects of the aerospike attached to payload fairing are studied with velocity and density plots. The schlieren pictures, oil flow and the pressure measurements on an aerospike attached to the payload fairing are analyzed and compared with the present numerical results with the Mach number in the range of $0.8 \leq M_\infty \leq 3.0$ and freestream Reynolds number range $33.35 \times 10^6/\text{m} \leq Re \leq 46.75 \times 10^6/\text{m}$. The present Mach number range covers the maximum drag and dynamic conditions during the ascent flight of the typical satellite launch vehicle. A distinct flowfield is found for $M_\infty < 1$ and $M_\infty > 1$ with and without the aerospike attached to the payload fairing. Flow separation is found at all freestream Mach numbers over the aerospike with the recirculation zone being Mach number dependent. As the freestream Mach number increases the separation zone becomes steeper. It is found that the aerospike attached to the payload fairing leads to drag reduction.

References

Ahmed, M.Y.M. and Qin, N. (2010a), "Drag reduction using aerodisks for hypersonic hemispherical

bodies", *J. Spacecraft Rockets,* **47**(1), 62-81. https://doi.org/10.2514/1.46655.
Ahmed, M.Y.M. and Qin, N. (2011b), "Recent advances in the aerothermodynamics of spiked hypersonic vehicles", *Prog. Aerosp. Sci.*, **47**(6), 425-449. https://doi.org/10.1016/j.paerosci.2011.06.001.
Baldwin, B.S. and Lomax, H. (1978), "Thin layer approximation and algebraic model for separated turbulent flow", *Proceedings of the 16th Aerospace Sciences Meeting*, Huntsville, Alabama, U.S.A., January.
Chang, P.L. (1970), *Separation of Flow*, Pergamon Press, Oxford, U.K.
Chung, K.M., Chang, P.H. and Chang, K.C. (2014), "Effect of Reynolds number on compressible convex-corner flows", *Adv. Aircraft Spacecraft Sci.*, **1**(4), 443-454. http://doi.org/10.12989/aas.2014.1.4.443
Daniels L.E. and Yoshihara, H. (1954), "Effect of the upstream influences of a shock wave at supersonic speeds in the presence of a separated boundary flows", WADC Tech. Rept., Wright Air Development Center, Air Research and Development Command, United States Air Force, U.S.A.
Das, S., Kumar, P., Ralh, M.K., Rao, R.K.M. and Prasad, J.K. (2013), "Drag reduction of a hemispherical body adopting spike at supersonic speed", *J. Aerosp. Sci. Technol.*, **65**(4), 313-325.
Deng, F., Liang, B., Xie, F. and Qin, N. (2017), "Spike effects on drag reduction for hypersonic lifting body", *J. Spacecraft Rockets*, **54**(6), 1185-1195. https://doi.org/10.2514/1.A33865.
Gerdroodbary, M.B. and Hosseinalipour, S.M. (2010), "Numerical simulation of hypersonic flow over highly blunted cones with spike", *Acta Astronaut.*, **67**(1-2), 180-193. https://doi.org/10.1016/j.actaastro.2010.01.026.
Haupt, B.F. and Koenig, K. (1987), "Aerodynamic effects of probe-induced flow separation on bluff bodies at transonic Mach numbers", *J. Spacecraft Rockets*, **24**(4), 327-333. https://doi.org/10.2514/3.25920.
Hillje, E.R. and Nelson, R.L. (1993), "Ascent air data system results from space shuttle flight test program", NASA CR 2283. Document ID: 19840002058.
Huang, W., Chen, Z., Yan, L., Yan, B. and Du, Z. (2019b), "Drag and heat flux reduction mechanism induced by the spike and its combinations in supersonic flows: A review", *Prog. Aerosp. Sci.*, **105**, 31-39. https://doi.org/10.1016/j.paerosci.2018.12.001.
Huang, W., Li, L., Yan, L.Q. and Zhang, T.T. (2017a), "Drag and heat flux reduction mechanism of blunted cone and aerodisks" *Acta Astronaut.*, **136**,168-178. https://doi.org/10.1016/j.actaastro.2017.05.040.
Jameson, A., Schmidt W. and Turkel, E. (1981), "Numerical solution of Euler equations by finite volume methods using Runge-Kutta time-stepping scheme", *Proceedings of the 14th Fluid and Plasma Dynamics Conference*, Palo Alto, California, U.S.A., June.
Jones, J.J. (1952), "Flow separation from rods ahead of blunt nose at Mach number 2.72", NACA RM, L52E05a, Document ID: 19930087040, National Advisory Committee for Aeronautics. Langley Aeronautical Lab, Langley Field, Virginia, U.S.A.
Kalimuthu, R., Mehta, R.C. and Rathakrishnan, E. (2019), "Measured aerodynamic coefficients of without and with spiked blunt body at Mach 6", *Adv. Aircraft Spacecraft Sci.*, **6**(3), 225-238. https://doi.org/10.12989/aas.2019.6.3.225.
Mair W.A. (1952) "Experiments on separation of boundary layers on probes in front of blunt-nosed bodies in a supersonic air stream", *Phil. Mag.*, **43**(342), 695-716. https://doi.org/10.1080/14786440708520987.
Mehta, R.C. (1997), "Numerical simulation of flow past spiked-nose heat shield", ASME-FED-SM 97-3293.
Mehta, R.C. (1998), "Flowfield over bulbous heat shield in transonic and low supersonic speeds", *J. Spacecraft Rockets*, **35**(1), 102-105. https://doi.org/10.2514/3.27004.
Mehta, R.C. (2002), "Numerical analysis of pressure oscillations over axisymmetric spiked blunt bodies at Mach 6.80", *Shock Waves*, **11**(6), 431-440. https://doi.org/10.1007/s001930200127.
Mehta, R.C. (2010a), "Numerical simulation of the flowfield over conical, disk and flat spiked body at Mach 6", *Aeronaut. J.*, **114**(1154), 225-236. https://doi.org/10.1017/ S0001924000003675.
Mehta, R.C. (2010b), "High speed flow field analysis for satellite launch vehicle and reentry capsule", *J. Magnetohydrodyn. Plasma Space Res.*, **15**(1), 51-99.
Mehta, R.C. (2017), "Multi-block structured grid generation method for computational fluid dynamics", *Scholars J. Eng. Technol.*, **5**(8), 387-393. https://doi.org/10.21276/sjet.
Mehta, R.C. and Jayachandran, T. (1997), "Navier-Stokes solution for a heat shield with and without a forward facing spike", *Comput. Fluids*, **26**(7), 741-754. https://doi.org/10.1016/S0045-7930(97)00011-X.

Menezes, V., Saravanan, S., Jagadeesh, G. and Reddy, K.P.J. (2009b), "Aerodynamic drag reduction using aerospike for large angle blunt cone flying at hypersonic Mach number", *Proceedings of the 22nd AIAA Aerodynamic Measurement Technology and Ground Testing Conference*, St. Louis, Missouri, U.S.A., June.

Mikhail, A.G. (1991), "Spike-nosed projectiles: Computations and dual flow modes in supersonic flight", *J. Spacecraft Rockets*, **28**(3), 418-424. https://doi.org/10.2514/3.26261.

Milicov, S.S. and Parlevic, D.M. (2002), "Influence of spike shape at supersonic flow past nosed bodies: Experimental study", *AIAA J.*, **40**(5), 1018-1020. https://doi.org/10.2514/2.1745.

Panaras, D. and Drikakis, D. (2009), "High speed unsteady flows around spiked-blunt bodies", *J. Fluid Mech*., **632**, 69-96. https://doi.org/10.1017/ S0022112009006235.

Piland, R.O. and Putland, L.W. (1954), "Zero-lift drag of several conical and blunt nose shapes obtained in free flight at Mach number of 0.7 to 1.3", NACA RM L54A27, Document Id: 19930089303, NACA Washington, U.S.A.

Purohit, S.C. (1986), "A Navier-Stokes solution for a bulbous payload shroud", *J. Spacecraft Rockets*, **23**(6), 590-596. https://doi.org/10.2514/3.25852.

Sahoo, D., Das, S., Kumar, P. and Prasad, J.K. (2016), "Effect of spike on steady and unsteady flow over a blunt body at supersonic speed", *Acta Astronaut*., **128**, 521-533. https://doi.org/10.1016/j.actaastro.2016.08.005.

Sebastian, J.J., Suryan, A. and Kim, H.D. (2016), "Numerical analysis of hypersonic flow past blunt bodies with aerospikes", *J. Spacecraft Rockets*, **53**(4), 669-677. https: //doi.org/10.2514/1.A33414.

Shoemaker, J.M. (1990), "Aerodynamic spike flowfields computed to select optimum configuration at Mach 2.5 with experimental validation", *Proceedings of the 28th Aerospace Sciences Meeting*, Reno, Nevada, U.S.A., January.

Srulijes, J., Runne, K. and Seiler, F. (2000), "Flow visualization and pressure measurements on spike-tipped blunt body", *Proceedings of the 1st Aerodynamic Measurement Technology and Ground Testing Conference*.

Venkateshan, M., Kannamanimuthu, N., Das, S., Kumar, P. and Prasad, J.K. (2011), "Flowfield investigation over a hemispherical blunt body with different spikes at supersonic speed", *Proceedings of the 38th National Conference on Fluid Mechanics and Fluid Power*, Bhopal, India, December.

Wang, Z.G., Sun, X.W., Huang, W., Li, S.B. and Yan, L. (2016), "Experimental investigation on drag and heat flux reduction in supersonic/hypersonic flows, A review", *Acta Astronaut*., **129**, 95-110. https://doi.org/10.1016/j.actaastro.2016.09.004.

White, J.T. (1993), "Application of Navier-Stokes flowfield analysis in the thermodynamic design of an aerospike configuration missile", *Proceedings of the California AIAAIAHS/ASEE Aerospace Design Conference*.

Yadav, R. and Guven, U. (2013), "Aerothermodynamics of a hypersonic projectile with a double-disk aerospike", *Aeronaut. J.*, **117**(1195), 913-928. https://doi.org/10.1017/ S0001924000008587.

Yamauchi, M., Fujii, K., Tamura, Y. and Higashino, F. (1995), "Numerical investigation of supersonic flows around a spiked blunt body", *J. Spacecraft Rockets*, **32**(1), 32-42. https://doi.org/10.2514/3.26571.

CC